Journal of Physics D: Applied Physics

PURPOSE-LED PUBLISHING™

PAPER

Electrode compensation strategy for etching-induced geometric deviations in high-frequency AT-cut quartz resonators

To cite this article: Fangmeng Xu *et al* 2026 *J. Phys. D: Appl. Phys.* **59** 205101

View the article online for updates and enhancements.

You may also like

- Design and Fabrication of Quartz MEMS Based Double-ended Tuning Fork Resonator
X. Bi, Y. Ma, X. Wang et al.

- Energy-trapping analysis for the bi-stepped mesa quartz crystal microbalance using the finite element method
F Lu, H P Lee and S P Lim

- A 3-Terminal AT-Cut Quartz Resonator with Shield Electrodes
Koichi Hirama, Yuji Aoyama, Matsutaro Naito et al.

This content was downloaded from IP address 223.112.146.162 on 14/06/2026 at 04:48

IOP Publishing J. Phys. D: Appl. Phys. **59** (2026) 205101 https://doi.org/10.1088/1361-6463/ae5f2c

Journal of Physics D: Applied Physics

Check for updates

RECEIVED
30 November 2025

REVISED
25 February 2026

ACCEPTED FOR PUBLICATION
14 April 2026

PUBLISHED
18 May 2026

PAPER

Electrode compensation strategy for etching-induced geometric deviations in high-frequency AT-cut quartz resonators

Fangmeng Xu, Kaiwen Chen, Chunyan Yin, Guangbin Dou* and Litao Sun*

SEU-FEI Nano–Pico Center, Key Laboratory of MEMS of the Ministry of Education Southeast University, Nanjing 210096, People's Republic of China

* Authors to whom any correspondence should be addressed.

E-mail: gdou@seu.edu.cn and slt@seu.edu.cn

Keywords: quartz resonator, high-frequency, inverted-mesa-type, etching-induced deviation, electrode compensation, impedance analysis

Abstract

Inverted-mesa-type quartz resonators are promising candidates for high-frequency and miniaturized applications. However, unavoidable geometric deviations introduced by wet etching alter the resonator's effective geometry and necessitate compensation strategies to stabilize its electrical performance. In this work, the initial resonator geometry is determined based on the thickness-shear vibration mechanism of AT-cut quartz crystal, and experimentally extracted sidewall inclination angles are incorporated to reconstruct the actual etched profile. The resulting reduction in the vibrating area and the structural asymmetry weakens energy confinement, causing a 4.91% downward shift in resonant frequency and a 49.99% reduction in quality factor. To mitigate these degradation effects, a two-step metal electrode compensation strategy is proposed. The electrode coverage ratio is first adjusted to counteract the frequency downward shift, and the mass-loading effect of the metal layer is subsequently utilized to fine-tune the effective thickness of the vibrating area. In addition, a simulated laser-trimming procedure is introduced, in which different electrode thicknesses are scanned to optimize the motional resistance and quality factor. By appropriately designing the electrode area and thickness, the motional resistance is reduced from 1830.5 Ω to 213.0 Ω while maintaining the target resonant frequency. The quality factor reaches 10 029, which lies within the acceptable performance range, demonstrating a substantial improvement in electrical performance. The established framework serves as a practical and extendable design tool for piezoelectric resonators affected by fabrication-induced geometric deviations.

1. Introduction

Quartz resonators are widely employed in communications and electronic systems owing to their piezoelectric properties, frequency stability, and long-term reliability (Fu *et al* 2025). Among various cuts of the quartz crystal (Jin *et al* 2019), the AT-cut quartz crystal operates in a thickness-shear mode, in which the resonant frequency is primarily determined by the wafer thickness, and a thinner wafer corresponds to a higher operating frequency (Zhu *et al* 2021). Driven by the growing requirements of high-speed communication and data transmission systems, stable reference clocks with high frequency and low phase noise are in strong demand (Salzenstein 2016). For example, in high-speed optical communication systems, quartz resonators are widely employed as stable reference clock sources in the hundreds-of-megahertz range (Grutter 2013). Similarly, high-frequency reference clocks are employed in automotive electronics, where quartz resonators are employed to support high-speed in-vehicle communication and sensing networks (Oliveira Fernandes Moreira 2015). To meet high-frequency requirements without globally thinning the quartz crystal and thereby compromising mechanical strength, inverted-mesa-type quartz resonators (Pao *et al* 2024) are adopted to achieve a locally thinned vibration region while maintaining mechanical robustness.

© 2026 IOP Publishing Ltd. All rights, including for text and data mining, AI training, and similar technologies, are reserved.

In addition to quartz resonators, high resonant frequencies can also be achieved using thin-film bulk acoustic resonators (FBARs) made of piezoelectric materials such as $LiNbO_3$ (Fang *et al* 2020) and AlN (Wingqvist 2010). Accordingly, in FBAR devices, the electrode-covered area is commonly assumed to coincide with the effective vibration region (Lu *et al* 2025), and mass loading effect is employed as a primary mechanism for frequency tuning and performance optimization (Lee *et al* 2004). Both the FBAR devices and the quartz resonators are typically fabricated using Micro-Electro-Mechanical Systems (MEMS) technology (Feng *et al* 2022). In MEMS technology, wet etching processes are used to fabricate the outer shape of the resonator due to their advantages of high efficiency and low cost (Li *et al* 2023b). However, quartz exhibits strong crystallographic anisotropy, and its wet etching behavior is highly sensitive to crystal-axis orientation, etchant chemistry, and surface morphology. As a result, the anisotropic wet etching of quartz crystal intrinsically reshapes the effective vibration region, leading to deviations between the actual resonating geometry and the idealized electrode-defined region, rendering design assumptions commonly used for FBARs no longer strictly applicable. The etched profiles of the quartz resonators therefore exhibit non-vertical sidewall angles and inconsistent shrinkage of the top and bottom openings, which leads to structural asymmetry. Such asymmetry shifts the effective vibration center, weakens lateral energy trapping (Kvashnin and Sorokin 2021), increases the likelihood of mode coupling (Li *et al* 2025) and parasitic-mode excitation (Cheng *et al* 2023). These effects manifest as performance degradation of key electrical properties, including resonant frequency, motional resistance, and quality factor, ultimately compromising the electrical performance of high-frequency quartz resonators (Kvashnin and Sorokin 2021).

Most existing studies on etching deviation modeling and compensation methods have focused on silicon-based microstructures. In contrast, compensation research for quartz wet etching on electrical performance remains limited. Dong proposed a mask-compensation method to address the size effects caused by trench width and spacing (Dong *et al* 2024). Studies on compensation strategies for quartz wet etching remain primarily at the geometric-compensation level, and existing works rarely address the coupled influence of realistic fabrication-induced geometry and electromechanical interactions on device performance. In this context, recent studies have demonstrated that embedding realistic device geometry into high-fidelity, multiphysics finite-element modeling (FEM) frameworks can improve the consistency between numerical predictions and actual device behavior. For example, Volpe *et al* employed a digital-twin-based modeling strategy for $LiNbO_3$-based surface acoustic wave devices to capture the electromechanical response under realistic operating conditions (Sfregola *et al* 2025). By contrast, systematic studies that integrate geometric compensation with electromechanical performance modeling remain limited.

This study incorporates etching-induced sidewall inclination into FEM-based modeling of quartz resonators. By accounting for structural asymmetry and electrode placement induced by etching deviations, and further optimizing electrode dimensions through the mass-loading effect, the proposed design maintains thickness-shear-mode vibration near the target frequency while minimizing performance deterioration. Simulation results demonstrate that the motional resistance is reduced from 1830 Ω to 213 Ω, confirming the effectiveness of the proposed approach in significantly improving the electrical performance of miniaturized quartz resonators.

2. Theory

2.1. Material properties and coordinate transformation of AT-cut quartz crystal

2.1.1. Crystal properties of AT-cut quartz crystal

Before establishing the geometry model of the inverted-mesa-type quartz resonator, the material properties of the quartz crystal and the coordinate transformation of the AT-cut quartz crystal need to be discussed. The ideal morphology of a quartz crystal is a regular hexagonal prism terminated by symmetric pyramids at both ends. In crystallography, the crystal orientation is commonly described using three mutually orthogonal axes, as illustrated in figure 1(a), namely the X-axis, Y-axis, and Z-axis. The X-axis of a quartz crystal is referred to as the electrical axis (Saigusa 2010). When compressive or tensile stress is applied along the X-axis, a piezoelectric effect is generated in the same direction. The y-axis is known as the mechanical axis (Ramon 2014). When stress is applied along the Y-axis, no piezoelectric effect is produced, and only mechanical deformation occurs. The z-axis is referred to as the optical axis. When light propagates along the Z-axis through the quartz crystal, optical birefringence does not occur. The high-frequency quartz resonators are typically fabricated using AT-cut and SC-cut quartz crystals.

Figure 1(b) shows the definition method of the rotating coordinate system in the COMSOL Multiphysics software. COMSOL Multiphysics defines three consecutive rotations from the global axis

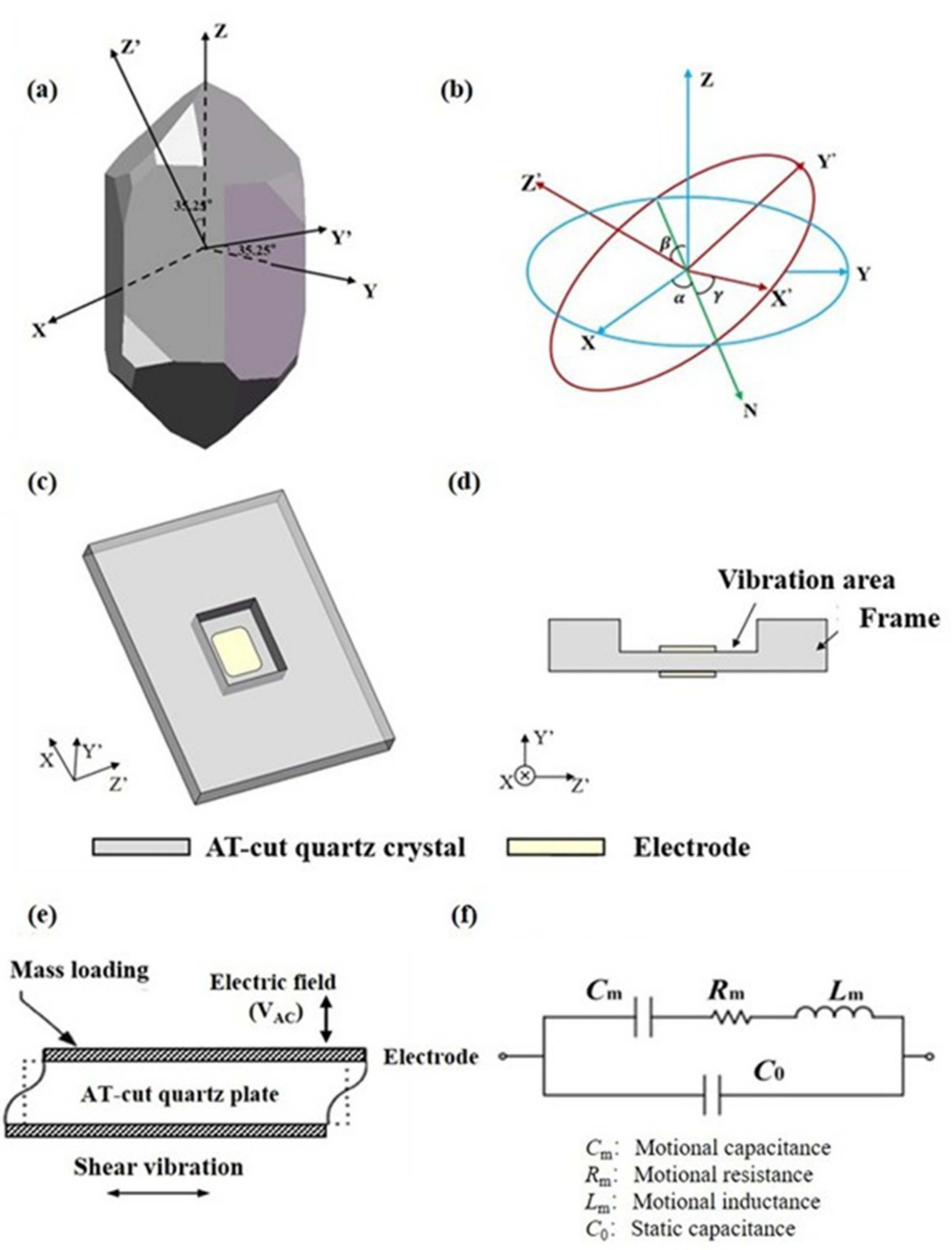

Figure 1. Illustration of AT-cut quartz crystal and inverted-mesa-type quartz resonator, (a) schematic structure of quartz crystal and the AT-cut rotation illustration, (b) Euler-angle rotation used in COMSOL Multiphysics, (c) schematic diagram of an inverted-mesa-type quartz resonator, (d) cross section along the X-axis, (e) schematic illustration of the thickness-shear mode vibration of AT-cut quartz crystal and the mass loading effect, (f) the BVD equivalent circuit model.

(X, Y, Z) to the crystal axis (X', Y', Z') using Euler angles (α, β, γ). For AT-cut quartz crystals, the rotation angle is approximately $\alpha \approx 35°$. Figure 1(c) is a schematic diagram of the inverted-mesa-type quartz resonator, including the frame and the metal electrodes. Figure 1(d) is the cross-sectional view of the resonator along the X-axis.

Due to different crystallographic cuts, quartz crystals exhibit different vibration modes (Zhu *et al* 2019). When an alternating electric potential is applied to the metal electrodes of an AT-cut quartz plate, an electric field is generated across the thickness of the resonator (Satani *et al* 2022). Owing to the piezoelectric effect of quartz, the electric field induces shear stress within the crystal, resulting in shear deformation. The shear deformation is characterized by the elongation along one diagonal direction and contraction along the other diagonal direction. Since the shear deformation involves shear motion across the thickness of the resonator, the corresponding vibration mode is referred to as the thickness-shear vibration mode (Zhu *et al* 2021), as illustrated in figure 1(e).

When the thickness of the vibration area is much smaller than its length and width, the frequency equation (Saigusa 2010) is expressed by

$$f = \frac{1}{2h}\sqrt{\frac{c_{66}}{\rho}}, \tag{1}$$

where h is the thickness of the quartz plate. The elastic stiffness constant of quartz c_{66} is 29.01 GPa. The density of quartz ρ is 2649 kg m^{-3} (Ramon 2014). Based on the above theoretical analysis, the thickness of the vibration region corresponding to a target resonant frequency of 96 MHz is calculated to be 17.24 μm. Considering the influence of the metal electrodes on the resonant frequency, the thickness is initially set to 17 μm in the resonator design and analysis.

2.2. Electrical characteristics of quartz resonator

Before proceeding to the detailed analysis of the resonator behavior, it is essential to clarify several key electrical parameters that are commonly used to evaluate quartz resonators, namely the impedance characteristics, motional resistance, and quality factor. These parameters are inherently connected through the Butterworth–Van-Dyke (BVD) equivalent model (Muramatsu *et al* 1988) and form the basis for interpreting both simulated and measured electrical responses.

As shown in figure 1(f), the electrical behavior of a quartz resonator is commonly interpreted based on the BVD equivalent model (Larson *et al* 2000). Although the detailed circuit parameters are not the focus of this work, the BVD model indicates that the resonator exhibits a series resonant frequency f_{s}, corresponding to the minimum impedance, and a parallel resonant frequency f_{p}, where the impedance reaches a maximum due to the interaction between the motional arm and the static capacitance (Chen and Wu 2000).

The impedance magnitude and phase responses are therefore used to identify the resonant mode. At f_s, the phase crosses zero, indicating a transition from capacitive to inductive behavior (Sun *et al* 1996). This characteristic phase reversal is particularly useful for locating resonance in high-frequency quartz resonators. In this work, impedance analysis is employed to extract the resonant frequency and to confirm that the simulated mode corresponds to the fundamental thickness-shear vibration.

In the BVD model, the motional resistance R_1 characterizes the energy loss of the resonator and corresponds to the minimum impedance at f_s (Zhang *et al* 2025). This parameter is widely used as an indicator of the resonator's performance, especially in high-frequency designs.

The quality factor (Q factor) of a quartz resonator is defined as the ratio of stored energy to dissipated energy (Zimmermann *et al* 2001 a). The maximum value for Q is limited by the intrinsic material constants (Pogrebnyak and Abdrafikov 1992). The Q-factor can also be calculated using the BVD parameters R_1 (resistance), L_1 (inductivity), and C_1 (capacity), expressed as (Behling *et al* 1997):

$$Q = \frac{\omega L_1}{R_1} = \frac{1}{\omega R_1 C_1}. \tag{2}$$

2.3. Model assumptions

To reduce computational complexity while retaining physical accuracy, assumptions are introduced before numerical modeling, including the thin-electrode assumption and the surface mass loading effect.

2.3.1. Thin-electrode assumption

In practical resonator fabrication, the electrode thickness h' is typically two to three orders of magnitude smaller than the crystal thickness h. For AT-cut quartz resonators operating in the tens to hundreds of megahertz range, the thickness of the vibrating region is on the order of several to tens of micrometers, whereas the metal electrode thickness is usually on the order of tens to hundreds of nanometers, which is consistent with the commonly adopted thin-electrode assumption in the modeling. Therefore, the effect of electrode thickness on the overall resonator's mechanical stiffness can be neglected, and the electrode layer can be treated as a surface boundary condition rather than an explicit solid domain (Dai *et al* 2018). This simplification substantially reduces computational cost without sacrificing accuracy in predicting frequency and impedance behavior.

2.3.2. Mass loading effect

The presence of metal electrodes on the quartz resonator surface introduces an additional inertial effect, which leads to a shift in the resonant frequency. This phenomenon is commonly referred to as the mass loading effect (Huang *et al* 2022).

Under the thin-electrode assumption, the mechanical influence of the electrodes is primarily manifested through their inertial contribution rather than their elastic stiffness. As shown in figure 1(f), the additional mass contributed by the metallic electrodes alters the resonant frequency of the quartz plate. Instead of explicitly modeling the electrode layers, the surface mass loading effect introduces an equivalent surface mass

$$\Delta m = 2\rho' h' S \tag{3}$$

area on the electrode-covered regions, where ρ' is the density of the electrode material and h' is the electrode thickness (Huo *et al* 2023). For AT-cut quartz resonators, surface mass loading introduces a perturbation to the resonant frequency, which can be evaluated using a first-order approximation. Accordingly, the frequency shift can be estimated as (Huang *et al* 2022)

$$\Delta f = -\frac{2{f_0}^2 \Delta m}{S\sqrt{\rho\mu}}, \tag{4}$$

where f_0 is the resonant frequency of the unloaded quartz plate, S is the effective vibration area, ρ is the density of quartz crystal, and μ $(= 2.947 \times 10^{10}\mathrm{Nm}^{-2})$ is the shear modulus of the AT-cut quartz crystal (Hu *et al* 2022).

3. Numerical modeling

3.1. Resonator structure design and initial electrode parameters

Before wet etching, the geometric model of the inverted-mesa-type quartz resonator needs to be determined. Figure 2(a) illustrates the modeled quartz resonator and its cross-section. The structural parameters of the resonator without electrodes are listed in table 1. According to equation (1), the thickness of the vibration region is set to 17 μm to achieve a resonant frequency of 96 MHz. To suppress spurious modes, a sweep of the length-to-thickness ratio is performed, and the optimal ratio ensures modal isolation while keeping the frequency deviation below 0.01 MHz. With this selected geometry, the resonator vibrates predominantly in the thickness-shear mode, enabling stable operation at 96 MHz.

Based on the optimized length-to-thickness ratio, the geometric parameters of the resonator's vibration region are determined. Then, in the electrode design of the inverted-mesa-type resonator, the size reduction of the resonator and the target frequency need to be paid attention. The electrode effect primarily encompasses the electrode's mass loading effect and relative stiffness (Dai *et al* 2018). The mass ratio R is defined as (Ji *et al* 2016)

$$R = \frac{2\rho' h'}{\rho h}, \tag{5}$$

where ρ', h', ρ and h represent the electrode density, electrode thickness, quartz density, and quartz thickness, respectively.

For a quartz plate with symmetric electrodes applied to both sides, as depicted in figure 2(c), the thickness of the quartz plate and electrodes is given by

$$h = 2b, \tag{6}$$

$$h' = 2b'. \tag{7}$$

An AT-cut quartz crystal and aurum electrodes with the following constants are considered to evaluate the effect of electrodes at a more extensive mass ratio. $c_{66} = 29.01 \times 10^9 N/m^2$, ${k_{26}}^2 = 7.81 \times 10^{-3}$, $\rho = 2649 kg/m^3$, $c'_{66} = 4.37 \times 10^{10} N/m^2$, $\rho' = 19320\ kg/m^2$.

The thickness-shear displacements, which satisfy the continuity boundary conditions on the interfaces, are given by

$$u_1 = A\sin\eta x_2, -b \leqslant x_2 \leqslant b, \tag{8}$$

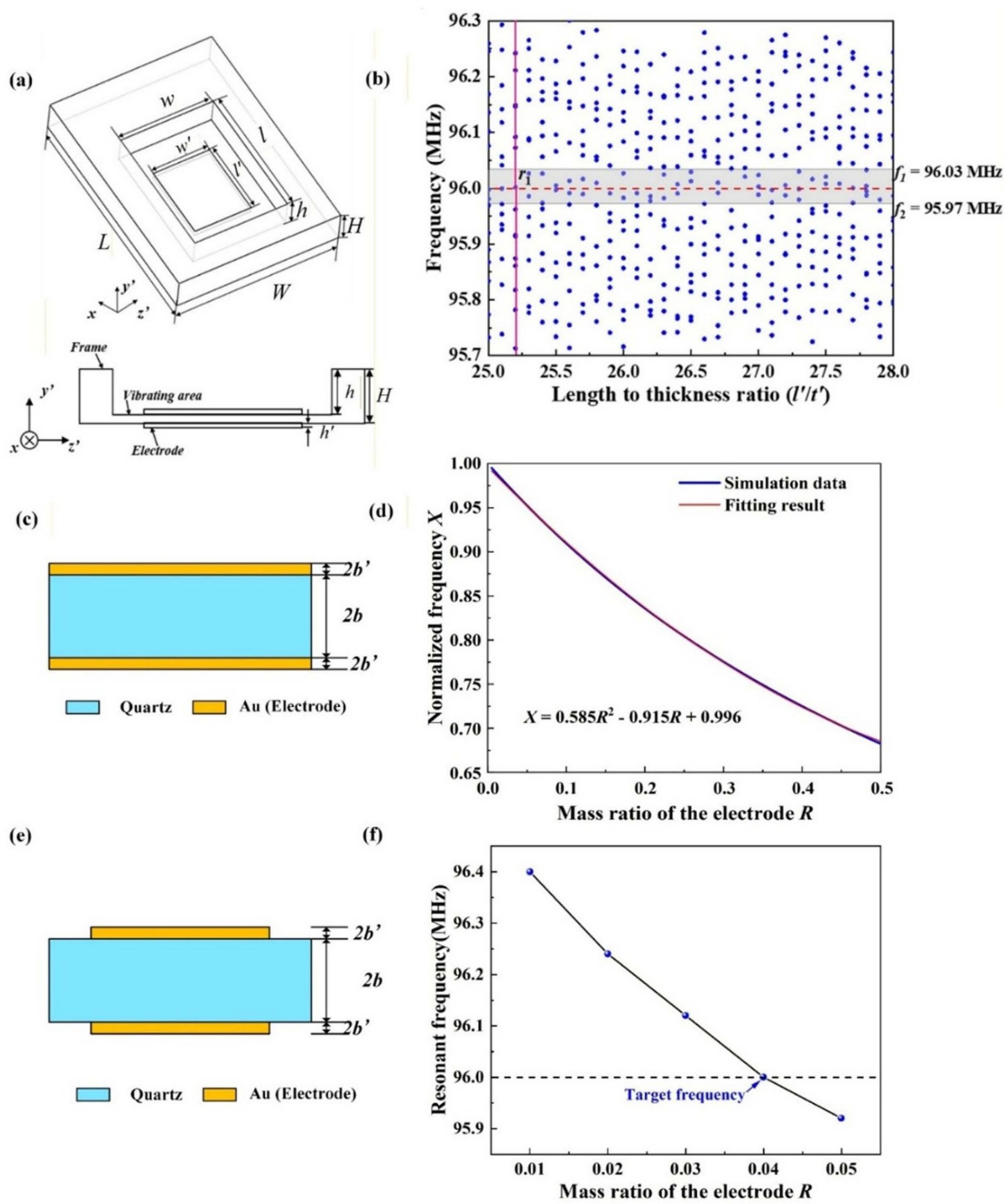

Figure 2. Structural schematic and frequency-related analyses of the inverted-mesa-type quartz resonator. (a) Overall structure of the inverted-mesa-type quartz resonator and the cross-section view along the X-axis, (b) relationship between the length-to-thickness ratio and the resonator's frequency. (c) Schematic of the full electrode coverage, (d) variation of normalized frequency with the electrode mass ratio, (e) partial electrode coverage, (f) relationship between the mass ratio of the electrode mass ratio and the resonant frequency.

$$u_1' = \pm A \sin\eta \cos \eta' (x_2 \mp b) + \bar{B} \sin\eta' (x_2 \mp b), \; b \leqslant x_2 \leqslant b + 2\bar{b}, \tag{9}$$

for the quartz crystal and electrodes, respectively, with wavenumbers in the crystal plate and electrodes denoted as η and η'.

The displacement amplitude A and $\bar{B}$ are introduced to define the boundary conditions. Therefore, the stress components corresponding to these displacements are given by

$$T_6 = c_{66}\, A\, \eta \cos\eta x_2, \tag{10}$$

$$T_6' = c_{66}' \eta' \left[\mp A \sin\eta b \sin\eta' (x_2 \mp b) + \bar{B} \sin\eta' (x_2 \mp b)\right], \tag{11}$$

Table 1. Structural parameters of the inverted-mesa-type quartz resonator without electrodes.

Symbol	Definition	Value (μm)
L	Length of the resonator	741
l	Length of the vibration region	426.6
W	Width of the resonator	546
w	Width of the vibration region	313
H	Depth of the resonator	100
h	Depth of the vibration region	17
l'	Length of the electrode	125
w'	Width of the electrode	91
h'	Depth of the electrode	0.1

where c_{66} and c_{66}' are elastic constants in the crystal and electrodes, respectively. For an infinite plate, the stress equations of motion for both the quartz crystal and the electrode layers can be written in terms of the displacement field and the corresponding stress components. Considering the thickness-shear vibration mode, the vibration is confined to the thickness direction of the resonator. By substituting the thickness-shear displacement solutions in equations (8) and (9) and the stress expressions in equations (10) and (11) into the equations of motion, the dispersion relations are obtained as

$$\begin{aligned} c_{66}\eta^2 - \omega^2\rho = 0, \\ c_{66}'\eta^2 - \omega^2\rho' = 0, \end{aligned} \tag{12}$$

where ω is the circular frequency. ρ, and ρ' are the density of the crystal and the electrodes, respectively.

From traction-free boundary conditions,

$$\begin{aligned} &T_6' = 0,\ x_2 = \pm(2b' + b), \\ &T_6 = T_6',\ x_2 = \pm b, \end{aligned} \tag{13}$$

together with the stress components in equations (10) and (11), we have

$$\begin{aligned} &-\mathit{sin}\,\eta b \sin 2\eta' b' A + \cos 2\eta' b' B' \\ &\quad = 0, c_{66}\eta\cos\eta b A - c_{66}'\eta' B' = 0. \end{aligned} \tag{14}$$

For resonance to occur, the conditions need to be

$$\begin{vmatrix} -\sin\eta b \mathit{sin} 2\eta' b' & \cos 2\eta' b' \\ c_{66}\eta\cos\eta b & -c_{66}'\eta' \end{vmatrix} = 0. \tag{15}$$

Then, the definitions are simplified as follows:

$$\begin{aligned} \eta = k\eta', k^2 = \tfrac{\bar{v}_2{}^2}{v_2{}^2}, v_2{}^2 = \tfrac{c_{66}}{\rho}, \bar{v}_2{}^2 = \tfrac{c_{66}'}{\rho'}, \\ B = \tfrac{\bar{b}}{b}, C_{66} = \tfrac{c_{66}'}{c_{66}}, \xi = \eta b, S_{66} = 2BC_{66} \end{aligned} . \tag{16}$$

And the equation can be rewritten as

$$\tan\xi\,\tan\frac{2B}{k}\xi = \frac{k}{C_{66}}. \tag{17}$$

With the solution ξ for known parameters appearing in equation (17), the frequency solution is depicted as follows:

$$\begin{aligned} \omega = \tfrac{\pi}{2b}\sqrt{\tfrac{C_{66}}{\rho}}\tfrac{2\xi}{\pi} = \omega_0 X, \\ f = \tfrac{1}{4b}\sqrt{\tfrac{C_{66}}{\rho}}\tfrac{2\xi}{\pi} = f_0 X, \end{aligned} \tag{18}$$

where the normalized frequency solution is defined as $X = \frac{2\xi}{\pi}$. Finally, the frequency equation can be written as $\tan\frac{\pi}{2}X\tan\frac{\pi B}{k}X = \frac{k}{C_{66}}$.

Figure 2(d) depicts the relationship between the electrode's normalized frequency and mass ratio. As the mass ratio increases, the resonator's normalized frequency decreases. The electrode's normalized frequency and mass ratio data are fitted to a quadratic function with the expression $X = 0.585R^2 - 0.915\ R + 0.996$.

In the design of the quartz resonator, metal electrodes are often used to partially cover the vibration area, as shown in figure 2(e). When the electrode partially covers the vibration region, the ratio of mass coverage under partial electrode coverage R_p is given by equation (19)

$$R_\mathrm{p} = \frac{2\rho' h' S'}{\rho h S}, \tag{19}$$

where ρ', h', ρ and h represent the electrode density, electrode thickness, quartz density, and quartz thickness, respectively. S' is the dimension of the electrode's area, and S is the dimension of the vibration area. In this section, the theoretical analysis focuses on the vibration region and the electrode–thickness relationship. The effects of wire interconnection and system-level fabrication are not included at this stage and will be addressed in the fabrication-related section.

As shown in figure 2(f), the mass ratio of the metal electrode R varies from 0.01 to 0.05 in increments of 0.01. In the case of partially metal electrode coverage, the resonant frequency decreases as the electrode mass ratio increases. When the electrode mass ratio reaches 0.04, the resonator reaches the target resonant frequency of 96 MHz, corresponding to a metal electrode size of 91 μm $\times$ 125 μm. Considering that additional metallic structures such as pads and interconnects would introduce extra mass loading in the practical device, the electrode thickness was finally set to 90 nm. Accordingly, the thickness of the vibrating region was selected as 16.93 μm for subsequent structural modeling and fabrication-oriented analysis.

3.2. Compensation of etching-induced geometric deviations

With the initial geometry of the quartz resonator defined, further adjustments are made to accommodate fabrication constraints introduced by wet etching. In particular, the anisotropic etching behavior of AT-cut quartz induces inclined sidewalls, which alter the effective dimensions of the vibrating region. These geometrical deviations are incorporated into the simulation to improve model fidelity and enable more reliable prediction of resonant behavior. The resonator outline and vibrating region were defined by the MEMS processes (Feng *et al* 2022). The fabrication flow is illustrated in figure 3(a). Quartz wafers were cleaned using the piranha solution (H_2SO_4:H_2O_2 = 3:1) at 90 °C for 5 min, followed by rinsing with deionized water. The cleaned quartz wafers were then baked at 120 °C for 5 min to ensure a dry surface. A Cr/Au electrode structure, consisting of a Cr adhesion layer and an Au electrode layer, was deposited on both sides of the quartz wafer by magnetron sputtering under a base pressure below 1×10^{-5}Pa. The thicknesses of the Cr and Au layers were 10 nm and 150 nm, respectively. Standard photolithography was employed to define rectangular patterns. The Au layer was etched using an iodine/potassium iodide (I_2/KI) solution, followed by Cr layer etching with a mixed solution of ceric ammonium nitrate, nitric acid, and glacial acetic acid. The patterned AT-cut quartz wafers were subsequently subjected to wet etching in saturated NH_4HF_2 solution at 85 °C for 2.5 h, resulting in an etching depth of approximately 83 μm.

After finishing the wet etching process, sidewall inclination angles were measured via optical microscopy and directly incorporated into the simulation model to reflect actual etched geometries. Figures 3(b)–(d) are the profiles of the resonator's outlook and the resonator's vibration area along the X-axis. Figures 3(e)–(g) are the corresponding profiles along the Z'-axis. Significant anisotropic behavior was observed, with inclination angles measured as 35° along the X-axis and 33°/58° along the Z'-axis. Replacing ideal vertical sidewalls with these experimentally derived inclinations improves the fidelity of the finite element analysis and better predicts performance shifts.

Figure 4 presents the structural comparison between the ideal inverted-mesa-type quartz resonator and the deviation-incorporated model. As shown in figure 4(a), the ideal resonator has a symmetric structure, and the thickness of the vibration region is 17.29 μm. However, during the wet etching process, the anisotropic etching behavior of quartz inevitably leads to geometry deviations. Specifically, the vibration area becomes narrower, the vibration region experiences a lateral shift, and the effective thickness of the vibrating region changes.

As illustrated in figure 4(b), the depth of the vibration area decreases from 17.29 μm to approximately 17 μm, accompanied by lateral shrinkage of the vibrating region. Moreover, the presence of electrodes and pads further introduces a mass-loading effect, which causes additional frequency reduction. Figure 4(c) shows the deviation-incorporated resonator, in which the etched sidewall angles are explicitly

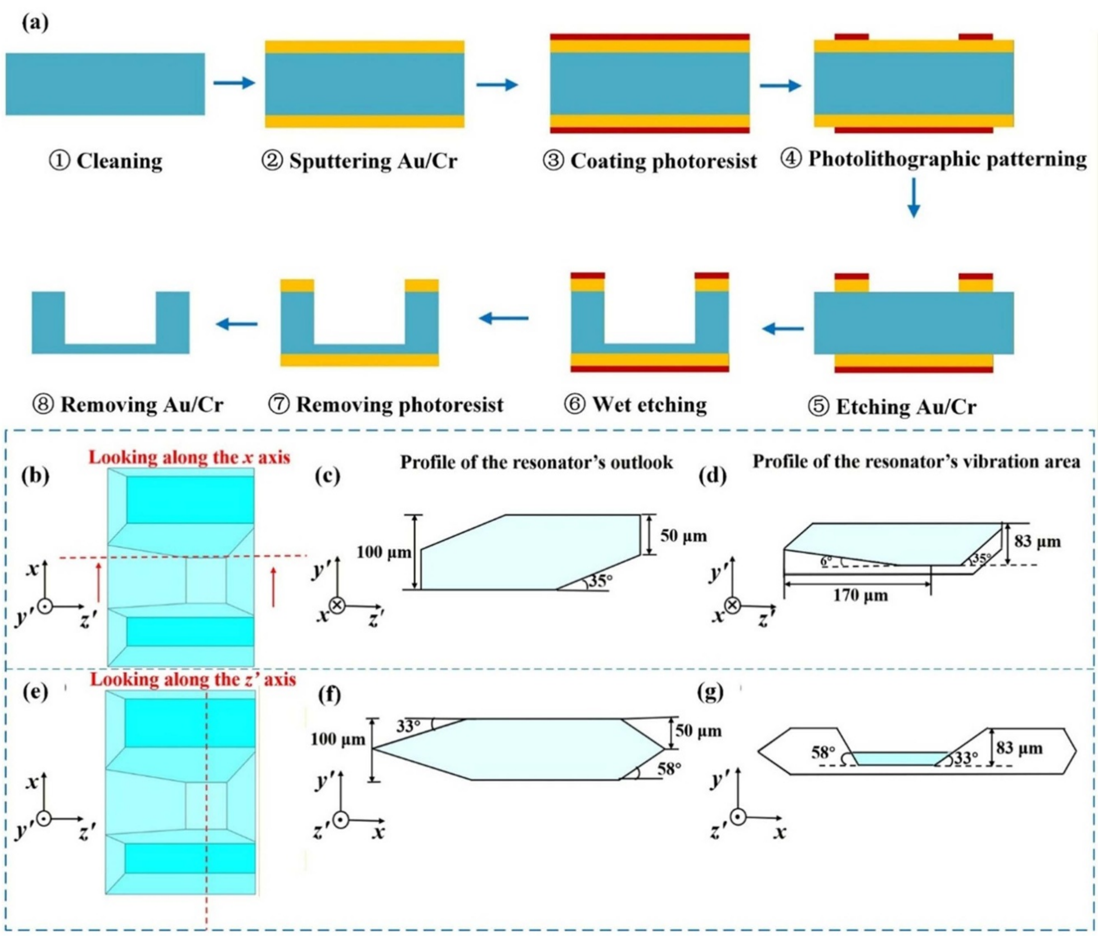

Figure 3. Wet etching process and the etching profiles of the quartz resonator. (a) Schematic illustration of the etching process, (b)–(d) overall profile and the resonator's vibration region along the X-axis, and (e)–(g) corresponding etched profiles along the Z'-axis.

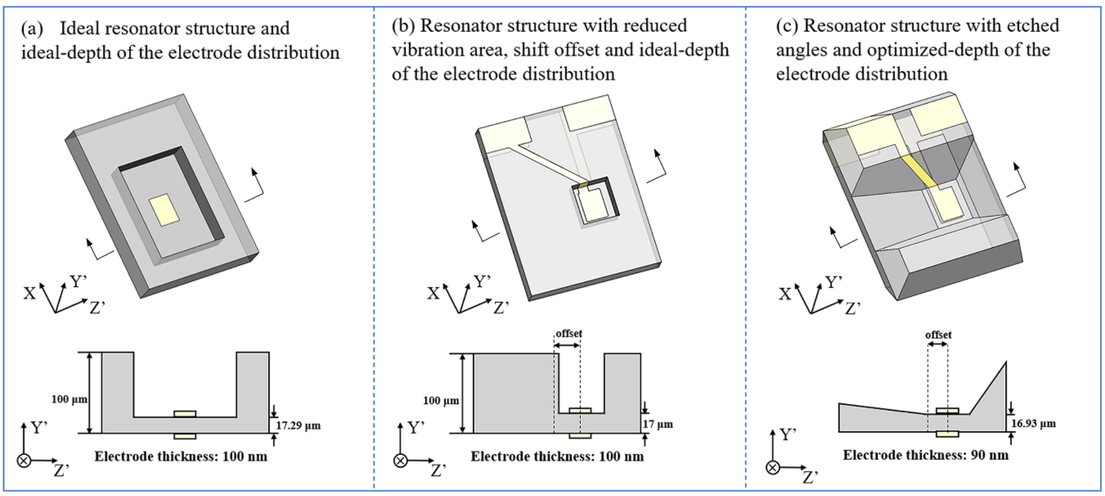

Figure 4. Structural comparison of quartz resonators before and after wet-etching-induced deviations. (a) Ideal structure and its cross-sectional view, (b) resonator structure with reduced effective vibration area and lateral shift caused by wet etching, (c) deviation-incorporated resonator with etched sidewall angles and the optimized electrode distribution for compensation.

included, and the electrode layout has been re-designed. The optimized electrode distribution accounts for both the reduced vibration area and the mass-loading effects, and the electrode thickness is adjusted from 100 nm to 90 nm to restore the target resonant frequency of 96 MHz.

Following the above geometric and electrical design considerations, the remaining step in completing the resonator layout is the electrical interconnection between the sidewall and bottom electrodes to enable signal routing and device excitation. In related quartz-resonator studies, this requirement is typically addressed using either stencil-mask-assisted angled metal deposition (Du *et al* 2017), where electrical continuity is achieved through geometric shadowing and oblique incidence during film growth, or patterned vertical metallization and routing (Iwata 2004), where dedicated metal traces are lithographically defined along the sidewall or frame region to connect the bottom electrode to the top-surface pads (Lee 2001). The former approach utilizes angled deposition with substrate rotation or multi-angle sputtering/evaporation to enable metallization on inclined sidewalls, whereas the latter relies on lithographically patterned metal traces for electrical interconnection. Since this study focuses on the influence of etching-induced geometry and electrode parameters on vibrational characteristics, the finite-element model applies electrical excitation directly to the electrode regions without explicitly including sidewall interconnects.

3.3. Electrode-based compensation strategy

With the resonator geometry defined to account for etching-induced geometrical features, a compensation strategy is needed to address the degradation in electrical performance caused by structural asymmetry. Figure 5 shows the flowchart of the electrode compensation strategy for deviation-induced performance degradation in inverted-mesa-type quartz resonators. After the shape of the metal electrodes is determined, the electrode thickness is further optimized. According to the mass-loading effect, the metal electrodes reduce the resonant frequency. In the absence of metal electrodes, the thickness of the vibration region is 17.29 μm. When the resonator includes metal electrodes, the resonant frequency deviates from the target value. Therefore, the electrode thickness needs to be adjusted so that the final resonant frequency approaches the target resonant frequency. It is important to note that the resonator includes not only the metal electrodes covering the vibration region but also the metal leads connected to the pads. These additional metal structures also affect the resonant frequency of the resonator.

By jointly adjusting the electrode shape and the electrode thickness, key electrical parameters of the resonator, including the resonant frequency, the motional resistance, and the quality factor, can be obtained. An electrode parameter set is then selected to balance these performance metrics for practical fabrication. Finite-element simulations are further used to assess mode purity, mode coupling, and variations in motional resistance and quality factor, thereby validating the effectiveness of the proposed electrode-compensation strategy.

3.4. Numerical simulation and validation

This work incorporates experimentally measured inclination angles into the geometric model and further analyzes their impact on impedance performance. The quartz resonator model is shown in figure 6(a), which consists of the AT-cut quartz crystal, electrodes (Au), and pads. The cross-sectional view along the X-axis is depicted in figure 6(b). The detailed parameters of the resonator are shown in table 2. The constitutive parameters of the AT-cut quartz crystal are specified based on the IEEE 1978 standard (Vig, 1992), and the crystallographic orientation was defined using the Euler-angle-based rotated coordinate system.

The simulation employed the 'Solid Mechanics' and 'Electrostatics' modules (Lu *et al* 2025). Fixed constraints are applied to the back-side pads of the resonator, while $\pm$2.5 V voltages were applied to both surfaces of the electrodes to excite the resonator. All remaining external surfaces were treated as mechanically free. Eigenfrequency analysis and frequency-domain analysis were performed. In the eigenfrequency analysis, the ARPACK eigensolver was used with a relative tolerance of 1×10^{-3}. In frequency-domain analysis, a harmonic sweep from 94 MHz to 98 MHz with a step size of 0.1 MHz was conducted using a relative tolerance of 0.001 to obtain the impedance response.

To ensure the reliability of the simulation results, a mesh refinement strategy was adopted. Based on the resonator geometry shown in figure 7(a), the overall thickness of the resonator is 100 μm, the thickness of the vibration region is about 16.93 μm, while the metal electrode thickness is only 100 nm (0.1 μm). Owing to the pronounced scale disparity between the vibration region and the ultra-thin metal electrodes, a uniform mesh refinement strategy was not applied throughout the entire device. Instead, a region-dependent meshing approach was employed. The model was discretized using free tetrahedral mesh elements, with a standard element size in the bulk region and finer elements introduced

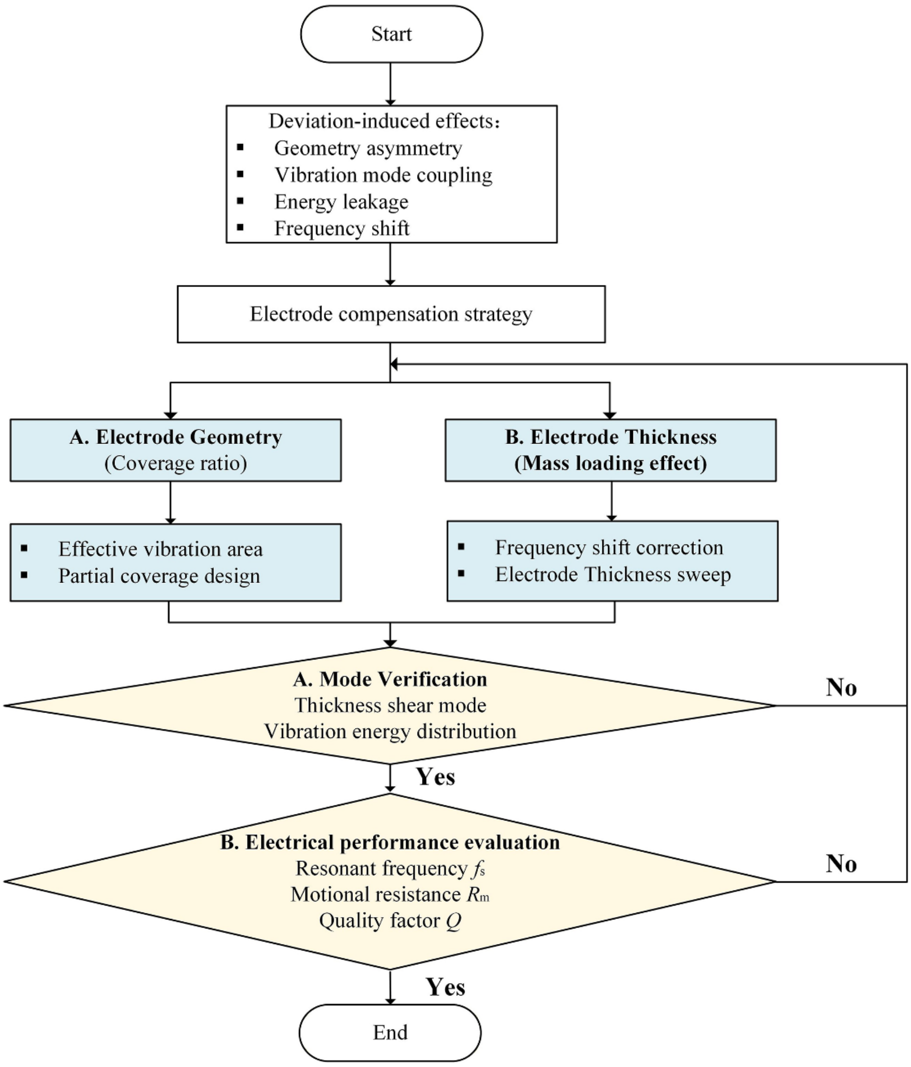

Figure 5. Flowchart of the electrode compensation strategy for deviation-induced performance degradation in inverted-mesa-type quartz resonators.

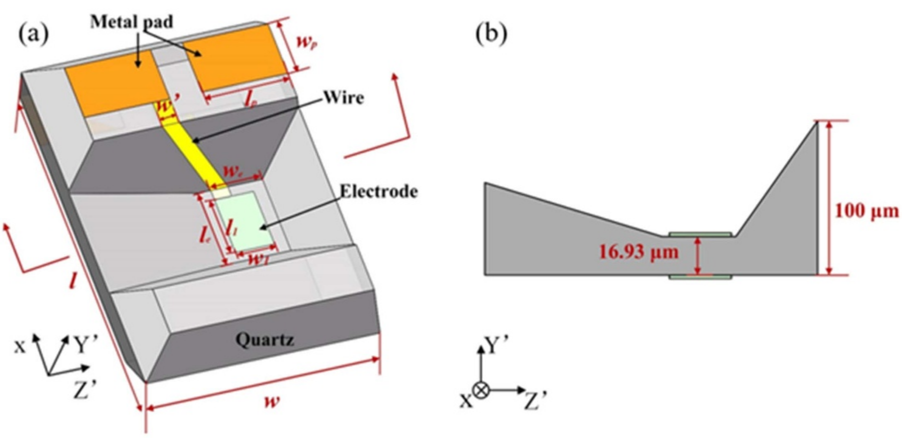

Figure 6. Geometry of the inverted-mesa-type quartz resonator with etching angles, (a) the resonator structure with etching deviations, (b) the cross-sectional view along the X-axis.

Table 2. Optimized structure parameters of the inverted-mesa-type quartz resonator.

Component	Symbol	Definition	Value	Unit
Profile of the resonator	l	Length	741	μm
	w	Width	546	μm
	t	Depth	100	μm
Profile of the vibrating region	l_e	Length	170	μm
	w_e	Width	150	μm
	t_e	Depth	16.93	μm
Pad	l_p	Length	200	μm
	w_p	Width	110	μm
Wire	w'	Width	40	μm
Electrode	l_1	Length	125	μm
	w_1	Width	91	μm
	t_1	Depth	90	nm

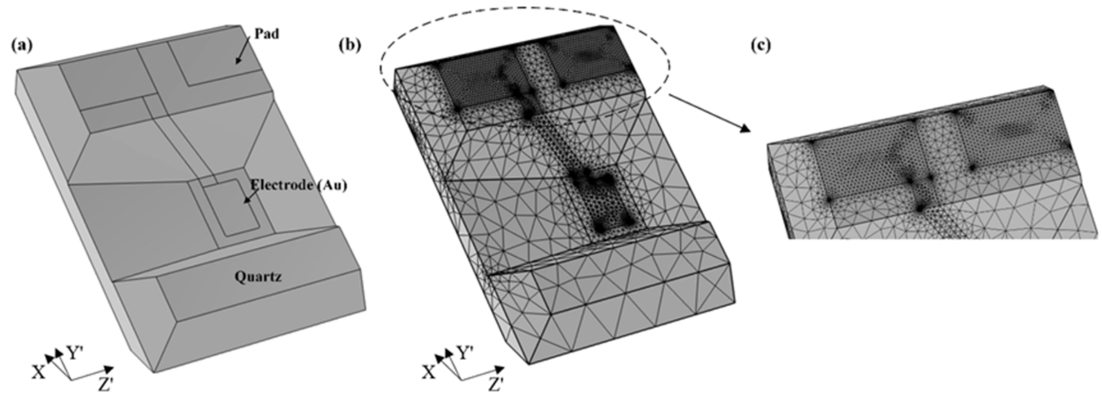

Figure 7. The establishment of the model and the subdivision of the grid. (a) Schematic diagram of the model, (b) mesh of the resonator model, (c) locally refined mesh in the electrode region.

near the electrode edges and bottom of the vibration area to resolve local stress concentrations and field variations. The global mesh and the refined mesh in the electrode region are presented in figure 7(b) and figure 7(c), respectively.

Using a non-uniform meshing strategy with region-specific refinement, the computational domain was discretized into approximately 85 817 elements, corresponding to about 5.3×10^5 degrees of freedom. Mesh quality was evaluated using the maximum angle and the volume-to-circumradius ratio as metrics, with average values of 0.614 and 0.454, indicating that the element shapes fall within an acceptable range for stable numerical computation. Mesh convergence was verified by progressively refining the mesh in the key regions, with the relative deviation of the target eigenfrequency remaining below 0.01%. Overall, the adopted meshing strategy ensures both numerical stability and sufficient resolution for the accurate evaluation of the resonator's electromechanical response.

4. Results and discussion

4.1. Mode analysis and impedance–frequency characteristics

To evaluate the influence of etching-induced structural deviations on resonator performance, mode analysis and impedance analysis were conducted for both the ideal structure and the geometry incorporating sidewall inclination (Kong *et al* 2024). The motional resistance (R_m) was extracted from the equivalent circuit fitting of the simulated admittance curve (Cao *et al* 2025), and the quality factor (Q) was calculated as $Q = f/\Delta f$, where f is the resonance frequency, and Δf is the -3 dB bandwidth. The Q factor is extracted from the simulated impedance response under idealized conditions, where air damping and

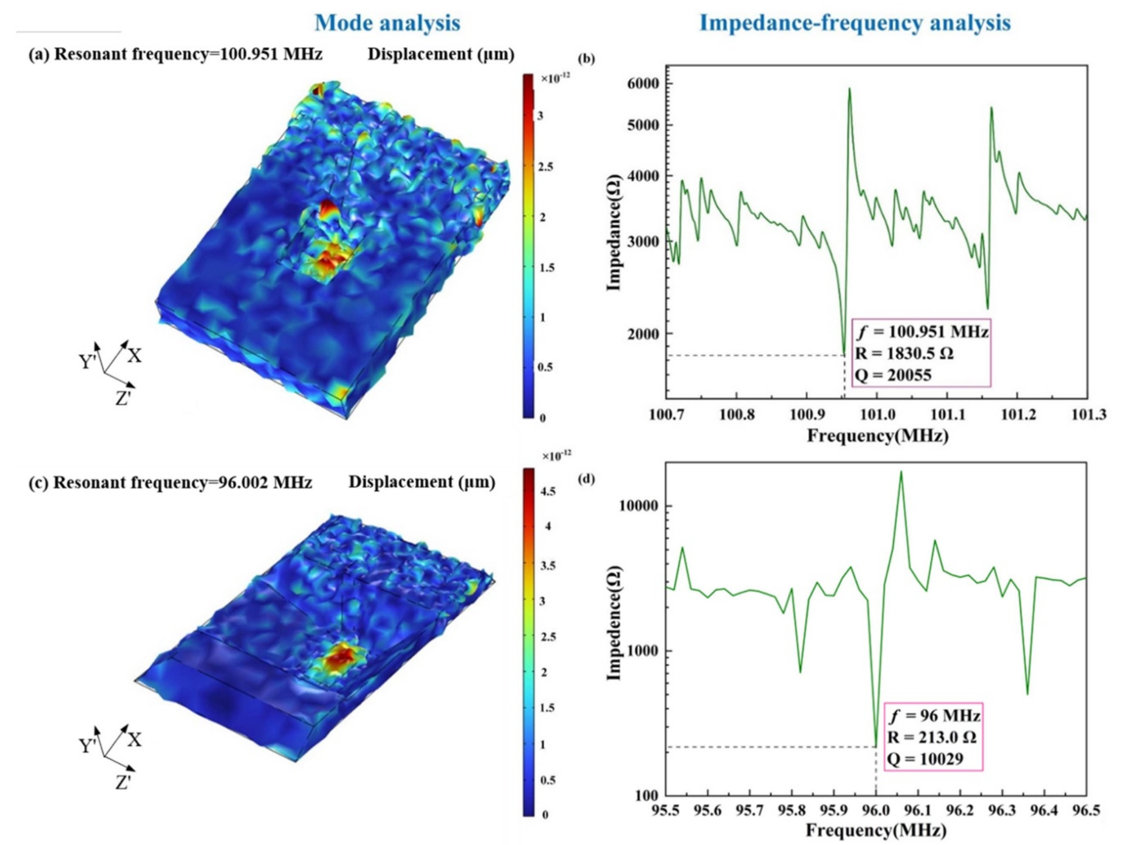

Figure 8. Mode analysis and impedance analysis of resonators, (a)–(b) simulated resonator model with ideal vertical sidewalls, (c)–(d) simulated resonator model with etching-induced sidewall inclination.

Table 3. Comparison of resonator performance before and after optimization.

Parameters	Before optimization	After optimization	Percentage of change
Resonant frequency f (MHz)	100.951	96.002	4.91%
Motional resistance R_m (Ω)	1830.5	213.0	88.36%
Quality factor Q	20 055	10 029	49.99%

packaging-related dissipation are not considered (Gerrard *et al* 2015). Thus, it represents an intrinsic, vacuum-like quality factor used for comparative analysis.

As shown in figure 8(a), the ideal structure supports a clear fundamental thickness-shear mode (Mashimo and Oba 2022), with energy concentrated at the center and rapidly decaying toward the edges, indicating strong spatial confinement and effective modal selectivity (Kvashnin and Sorokin 2021). However, anisotropic wet etching inevitably introduces sidewall inclination, resulting in symmetry-breaking geometrical perturbations. As shown in figure 8(c), the resonator still maintains the fundamental mode, but the resonant frequency shifts from 100.951 MHz to 96.002 MHz due to the reduced stiffness and altered effective mass distribution (Huo *et al* 2023).

The frequency–impedance response provides further insight. The comparison of the electrical performance is shown in table 3. In the ideal structure, as shown in figure 8(b), the simulated motional resistance reaches 1830.5 Ω with a quality factor of 20 755. The high impedance is primarily attributed to the unoptimized electrode configuration and the extremely small effective vibrating region, leading to poor electromechanical conversion efficiency (Wei *et al* 2022). To address this, the electrode geometry was optimized by tailoring the electrode geometry, including the shape, area, thickness, and pad layout (Boychuk *et al* 2022).

As shown in figure 8(d), the optimized structure exhibits a significantly reduced motional resistance of 213.0 Ω and a sharper resonance peak. This demonstrates that electrode design effectively enhances

Table 4. Resonator performance comparison.

References	Dimensions (mm × mm)	Frequency (MHz)	Motional resistance (Ω)	Quality factor
Liang *et al* (2013)	4 × 4	84	47.039	25 000
Zimmermann *et al* (2001 b)	12 × 8	75	/	50 000
Fernandez *et al* (2020)	0.762 × 0.762	149	/	12 000
Our study	0.741 × 0.586	96	213.0	10 029

the electromechanical coupling, even in the presence of structural deviations. Nevertheless, the quality factor decreased from 20 055 to 10 029, indicating increased energy dissipation associated with asymmetry in the resonator body (Humbert *et al* 2022). These results indicate that electrode optimization, although effective in reducing motional resistance, cannot fully recover the Q degradation induced by etching-related asymmetry.

In figures 8(b) and (d), several peaks appear in the vicinity of the main resonance. These adjacent peaks are attributed to flexural and in-plane vibration components induced by the device boundaries and lateral confinement (Sekimoto *et al* 1991), which are associated with short-wavelength vibrational energy extending into the non-electroded regions of the quartz resonator (Ma *et al* 2015). Previous studies have shown that the strength of spurious responses is closely related to the lateral geometric symmetry and the energy-trapping capability of the resonator. The sidewall inclination introduced by wet etching breaks the lateral geometric symmetry and modifies the effective electrode-coverage boundary conditions of the inverted-mesa structure, thereby weakening lateral energy confinement. As a result, the electrical response exhibits an increased number of spurious peaks, an elevated motional resistance, and a reduced quality factor, thereby degrading the frequency selectivity and stability of the resonator.

To objectively assess the value of the design method presented in this work, we compare several representative studies on quartz resonators. The comparison of electrical performance is summarized in table 4. As the resonator dimensions are reduced to within 1 mm × 1 mm, the resonant frequency can still reach above 100 MHz; however, the energy-trapping effect is weakened. From the electrical parameters perspective, the increased motional resistance observed in this study is primarily attributed to the reduced electrode area, since enlarging the electrode generally lowers the resistance by improving electromechanical coupling. Moreover, at relatively high motional resistance, the influence of connection pads, bonding wires, and packaging parasitics on device performance should be carefully evaluated, which represents a critical direction for future research.

Despite the moderate reduction of the quality factor to 10 000, the obtained quality factor remains sufficient for practical applications of quartz resonators. More importantly, the simulation-based design and optimization approach adopted in this study demonstrates that even under small-size constraints, the resonator can achieve reliable operation in high-frequency applications. The trends observed in our simulations are consistent with experimental reports, further validating the proposed framework.

In this study, the primary focus is on the impact of sidewall inclination and geometric deviations introduced by anisotropic wet etching on the electrical performance of quartz resonators. Surface roughness, which accompanies the etched surfaces, can introduce additional acoustic losses and affect the electrical response. Previous studies have reported that roughness may reduce the resonant frequency and promote mode coupling and spurious responses (Li *et al* 2023a). From an equivalent-circuit perspective, surface roughness can be interpreted as introducing additional loss paths associated with interfacial friction and viscous dissipation, leading to an increase in the effective series resistance and a degradation of the quality factor. Within the framework proposed in this work, the electrode-based compensation primarily targets the dominant degradation induced by sidewall inclination. Roughness-related effects can be incorporated as additional surface-morphology parameters in future extensions of the same modeling framework, although this is beyond the scope of the present study (kuroiwa and Nakazawa 2002).

4.2. Effect of structural asymmetry on vibrational energy distribution

To further clarify the physical mechanism behind the variation of motional resistance and quality factor, the physical mechanism is illustrated in figure 9. Figure 9(a) shows the cross-section of the quartz resonator under ideal geometry along the X-axis, where the center of the metal electrode coincides with that of the vibrating region, resulting in a symmetric electrode distribution. Figure 9(c) further illustrates the uniform electrode coverage under this symmetric condition. Under the symmetric condition, the vibrational energy is confined within the electrode-covered working area, leading to a dominant thickness-shear mode with minimal spurious excitation and a high quality factor.

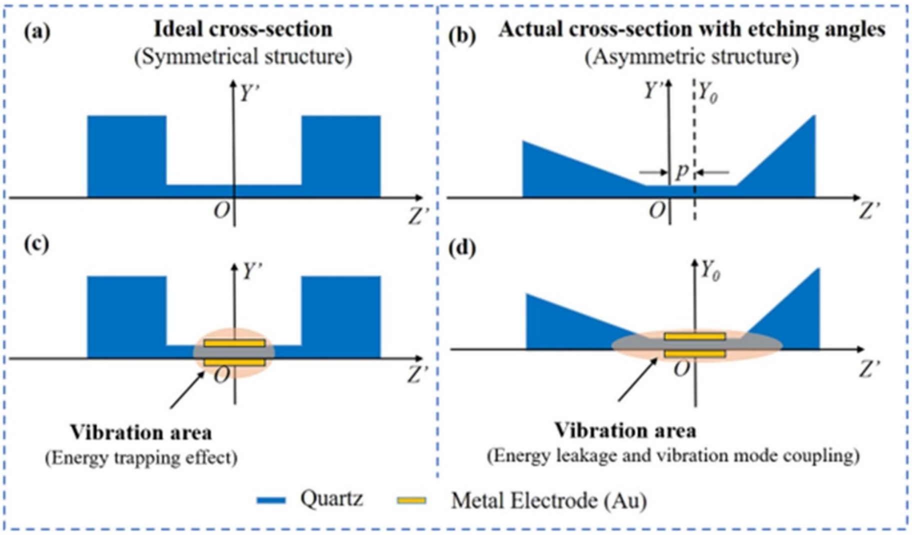

Figure 9. Vibration mechanism of inverted-mesa-type quartz resonators under ideal and etching-induced geometries. (a) Ideal cross-section of the resonator, (b) etching-induced cross-section, (c) vibration energy distribution in ideal geometry, (d) vibration energy distribution in etching-induced geometry. The dashed vertical line indicates the axis of symmetry ($Z = 0$), and the orange regions denote the vibration area of the resonator.

During the fabrication of miniaturized quartz resonators by wet etching, the anisotropy of quartz leads to deviations of the resonant region from the ideal geometry. Figure 9(b) shows the cross-section of an inverted-mesa-type quartz resonator with etching-induced deviation along the X direction. The center of the vibration region is offset from the geometric center of the resonator by a distance of p. As shown in figure 9(d), the center of the metal electrode cannot fully coincide with the center of the vibration region, resulting in an asymmetric electrode distribution. Under the asymmetric condition, the vibrational energy is no longer restricted to the central region but partially diffuses toward the edges and even leaks along the sidewalls. The altered energy distribution causes coupling of vibration modes and the excitation of additional parasitic modes, which increases acoustic dissipation and lowers the quality factor.

The degradation of resonator performance is fundamentally associated with changes in vibrational energy distribution. Comparisons between ideal and non-ideal structures highlight the critical roles of geometric symmetry and electrode configuration in maintaining energy trapping, thereby providing a physical basis for the electrode-based compensation strategy discussed in the following section.

4.3. Effect of electrode thickness on electrical characteristics

Since the electrode geometry has already been determined in the theoretical modeling and fixed by fabrication constraints, this subsection investigates electrode thickness as the primary adjustable parameter influencing the electrical characteristics of the resonator. To guide the parameter selection, practical performance criteria are first defined to ensure frequency accuracy and acceptable electrical performance. To simultaneously satisfy the combined requirements of a target frequency window, low R_{m}, and sufficient Q, the electrode thickness is screened by applying the following selection criteria:

- Frequency constraint is described as: $\left|f\left(t_1 - f_{\mathrm{target}}\right)\right| \leqslant \Delta f_{\mathrm{allow}}$,
- Impedance constraint is described as: $R_m\left(t_1\right) \leqslant R_m^{\max}$,
- Quality factor constraint is described as: $Q\left(t_1\right) \geqslant Q^{\min}$.

To evaluate the influence of electrode thickness on the resonant characteristics, a parametric study was conducted by varying the gold electrode thickness from 70 nm to 150 nm in steps of 10 nm. Figure 10(a) is the cross-section of the resonator along the X-axis. As shown in figure 10(b), increasing the electrode thickness causes a systematic downshift of the resonant frequency due to enhanced mass loading. Since the thickness of the vibrating region is defined by wet etching and the electrodes are subsequently deposited by sputtering, process fluctuations unavoidably introduce variations in electrode thickness and morphology. Consequently, the resonant frequency is evaluated in an allowable acceptance window rather than a single target value.

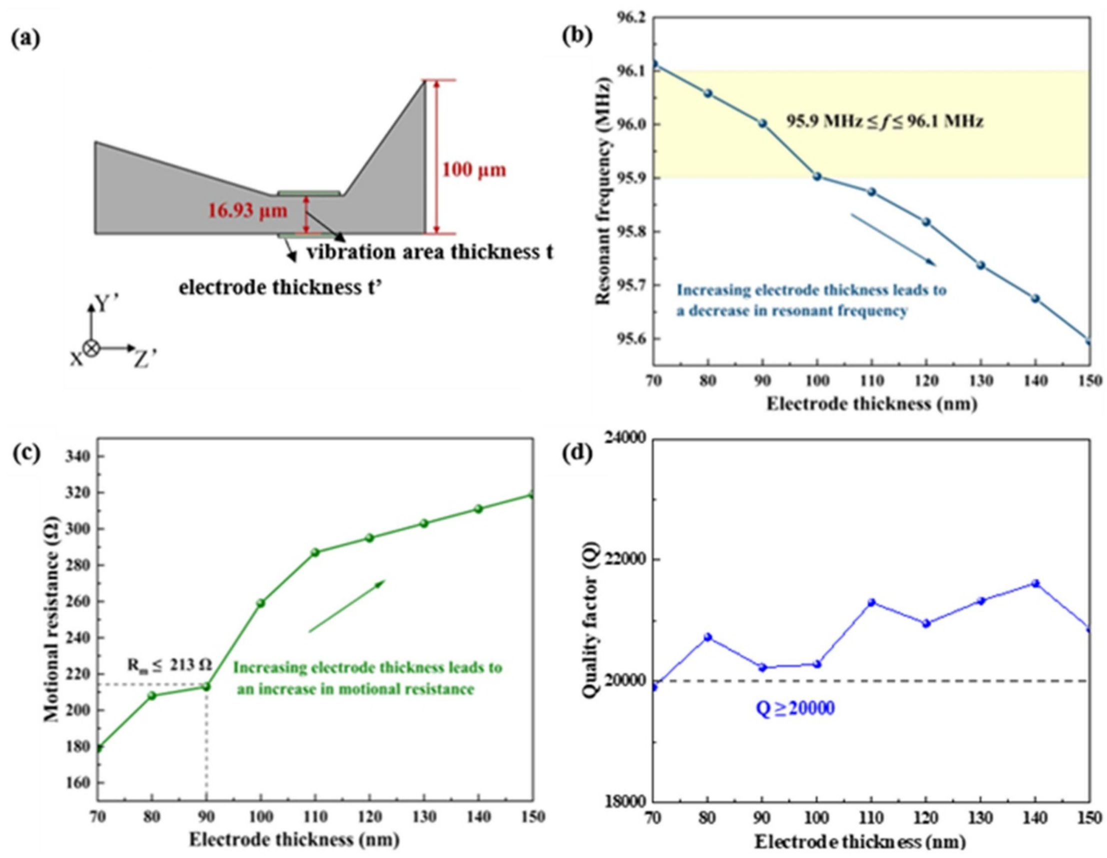

Figure 10. Electrode thickness dependence of electrical parameters, (a) cross-section of the resonator along the X-axis, (b) resonant frequency vs electrode thickness, (c) motional resistance versus electrode thickness, (d) quality factor versus electrode thickness.

To achieve the target frequency, industrial trimming techniques, such as laser trimming or dry-etching trimming, are commonly employed before packaging to exploit the mass-loading effect for fine correction. In this work, the acceptable frequency window is defined as ± 0.1 MHz around the target frequency, i.e. 95.9–96.1 MHz. Under this constraint, resonators with electrode thicknesses of 80 nm, 90 nm, and 100 nm all fall within the window and are retained as candidates for subsequent comparison and optimization of electrical performance. This acceptance window is consistent with reported frequency-trimming practices and can be readily integrated into mass-production inspection and trimming flows.

As shown in figure 10(c), the motional resistance of the resonator increases with the increase in the thickness of the resonator electrode. At an electrode thickness of 90 nm, the motional resistance reaches 213.0 Ω, beyond which a rapid increase is observed. Accordingly, $R_\mathrm{m} \leqslant 213\ \Omega$ is adopted as the design constraint. Figure 10(d) presents the variation of the quality factor with electrode thickness. In general, the quality factor exhibits a slight increasing trend as the electrode thickness increases. Since all candidate designs satisfy a practical requirement of $Q \geqslant 10,000$, the influence of electrode thickness on the quality factor is considered secondary in the parameter selection process.

5. Conclusion

In this work, a deviation-aware design framework is proposed for electrical performance compensation in high-frequency AT-cut quartz resonators. A parametric modeling and finite-element simulation flow implemented in COMSOL Multiphysics is developed to incorporate etching-induced geometric deviations and electrode mass-loading effects, enabling systematic optimization of resonant frequency, motional resistance, and quality factor. The results show that asymmetric sidewall inclination weakens modal confinement, leading to energy leakage, frequency degradation, and reduced quality factor.

A two-step electrode compensation strategy is introduced, combining coverage-based geometric correction with thickness-based mass-loading tuning to restore the target frequency and improve electrical performance. Finite-element simulations demonstrate that the proposed approach significantly reduces motional resistance and recovers the quality factor to an acceptable range, validating the engineering feasibility of the framework. Future work will focus on experimental validation, inclusion of additional fabrication deviations, and multi-objective optimization to further enhance the robustness of ultra-high-frequency quartz resonator design.

Data availability statement

All data that support the findings of this study are included within the article.

Conflict of interest

The authors declare no conflicts of interest.

Author contributions

Fangmeng Xu 0000-0003-0126-5732
Conceptualization (lead), Investigation (equal), Methodology (equal), Software (lead), Writing – original draft (lead)

Kaiwen Chen
Data curation (equal), Investigation (equal), Methodology (supporting), Software (supporting)

Chunyan Yin
Data curation (equal), Methodology (supporting), Writing – review & editing (supporting)

Guangbin Dou 0000-0001-8793-3441
Funding acquisition (lead), Methodology (equal), Project administration (lead), Supervision (lead), Writing – review & editing (lead)

Litao Sun 0000-0002-2750-5004
Funding acquisition (supporting), Project administration (supporting), Supervision (supporting)

References

Behling C, Lucklum R and Hauptmann P 1997 Possibilities and limitations in quantitative determination of polymer shear parameters by TSM resonators *Sens. Actuators A* **61** 260–6

Boychuk M I, Krivonogov V E, Mikaeva S A and Vasilieva L A 2022 Study of the reliability of quartz resonators in miniature ceramic packages *Russ. Technol. J.* **10** 43–50

Cao J, Li H, Wang H, Zhang H, Cao H, Wang X and Han Q 2025 Optimal design of vibration resistance of fiber-reinforced composite sandwich plates embedded in a viscoelastic square honeycomb core *Appl. Math. Modell.* **137** 115731

Chen P-C and Wu L 2000 The equivalent circuit of an AT-cut quartz resonator and its application *Jpn. J. Appl. Phys.* **39** 2710

Cheng J, Zhang Y, Long J and Li E 2023 A quasi-optical resonator with new coupling method and parasitic-mode-suppressing in 110–170 GHz *Electron. Lett.* **59** e12833

Dai X, Qian Z and Yang J 2018 A semi-analytical solution for electric double layers near an elliptical cylinder *Acta Mech. Sin.* **34** 62–67

Dong Y, Dou G, Wei Z, Ji S, Dai H, Tang K and Sun L 2024 Size-effect-based dimension compensations in wet etching for micromachined quartz crystal microstructures *Micromachines* **15** 784

Du K, Ding J, Liu Y, Wathuthanthri I and Choi C-H 2017 Stencil lithography for scalable micro-and nanomanufacturing *Micromachines* **8** 131

Fang Z, Jin H, Dong S, Lu L, Xuan W and Luo J 2020 Ultrathin single-crystalline $LiNbO_3$ film bulk acoustic resonator for 5G communication *Electron. Lett.* **56** 1142–3

Feng T, Yuan Q, Yu D, Wu B and WANG H 2022 Concepts and key technologies of microelectromechanical systems resonators *Micromachines* **13** 2195

Fernandez R, Calero M, Reiviakine I, Garcia J V, Rocha-Gaso M I, Arnau A and Jimenez Y 2020 High fundamental frequency (HFF) monolithic resonator arrays for biosensing applications: design, simulations, experimental characterization *IEEE Sens. J.* **21** 284–95

Fu M, Ma Z, Gao C, Ye Y, Li W, Hou D and Cao Y 2025 A multi-functional VOC sensor based on cascaded quartz crystal resonators *IEEE Electron Device Lett.* **46**, 476–9

Gerrard D D, Ng E J, Ahn C H, Hong V A, Yang Y and Kenny T W 2015 Modeling the effect of anchor geometry on the quality factor of bulk mode resonators *IEEE Transducers* 18th *Int. Conf. on Solid-State Sensors, Actuators and Microsystems* pp 1997–2000

Grutter K E 2013 Optical whispering-gallery mode resonators for applications in optical communication and frequency control *PhD thesis* University of California

Hu J, Yesilbas G, LI Y, Geng X, Li P, Chen J, Wu X, Knoll A and Ren T-L 2022 Exploration of the mass sensitivity of quartz crystal microbalance under overtone modes using electrodeposition method *Anal. Chem.* **94** 5760–8
Huang X H, Chen Q, Pan W and Yao Y 2022 Advances in the mass sensitivity distribution of quartz crystal microbalances: a review *Sensors* **22** 5112
Humbert C, Walter V and Leblois T 2022 A mass sensor based on digitally coupled and balanced quartz resonators using mode localization *Sens. Actuators A* **335** 113378
Huo Y, Wei Z, Ren S and Yi G 2023 High precision mass balancing method for the fourth harmonic of mass defect of fused quartz hemispherical resonator based on ion beam etching process *IEEE Trans. Ind. Electron.* **70** 9601–13
Iwata H 2004 Miniaturized ultrahigh-frequency fundamental quartz resonators *IEICE Electron. Express* **1** 346–51
Ji J, Zhao M, Ueda T and Ikezawa S 2016 Optimal design work for high-frequency quartz resonators *10th IEEE Int. Conf. on Sensing Technology* pp 1–4
Jin J, Zhang Y-M, Huang D-Y, Huang X-M and Hu H-P 2019 The optimization of an AT-cut quartz resonator with circular electrode *13th IEEE Symp. on Piezoelectricity, Acoustic Waves and Device Application* pp 1–4
Kong W, Fu T and Rabczuk T 2024 Improvement of broadband low-frequency sound absorption and energy absorbing of arched curve Helmholtz resonator with negative Poisson's ratio *Appl. Acoust.* **221** 110011
Kuroiwa M and Nakazawa M 2002 An analysis of plate surface roughness effect for AT-cut resonators *IEEE Int. Frequency Control Symp. & Pda Exhibition* pp 242–7
Kvashnin G and Sorokin B 2021 Peculiarities of energy trapping of the UHF elastic waves in diamond-based piezoelectric layered structure. II. Lateral energy flow *Ultrasonics* **111** 106311
Larson J D, Bradley P D, Wartenberg S and Ruby R C 2000 Modified Butterworth-van Dyke circuit for FBAR resonators and automated measurement system *IEEE Ultrasonics Symp.* pp 863–8
Lee J-B, Jung J-P, Lee M-H and Park J-S 2004 Effects of bottom electrodes on the orientation of AlN films and the frequency responses of resonators in AlN-based FBARs *Thin Solid Films* **447** 610–4
Lee S 2001 Photolithography and selective etching of an array of surface mount device 32.768 kHz quartz tuning fork resonators: definition of side-wall electrodes and interconnections using stencil mask *Jpn. J. Appl. Phys.* **40** 5480
Li M, Li P, Li N, Liu D, Kuznetsova I E and Qian Z 2023a Surface roughness effects on the vibration characteristics of AT-cut quartz crystal plate *Sensors* **23** 5168
Li Q, Zhang Y, Shi Z, Li W and Ye X 2023b Effect of different etching processes on surface defects of quartz crystals *Coatings* **13** 1785
Li Z, Jin G, Chen Y, Ye T, Zhang B, Yang T and LI P 2025 Unified vibration modeling of shell and plate structures with resonators *Int. J. Mech. Sci.* **287** 109921
Liang J, Huang J, Zhang T, Zhang J, Li X and Ueda T 2013 An experimental study on fabricating an inverted mesa-type quartz crystal resonator using a cheap wet etching process *Sensors* **13** 12140–8
Lu H, Hao X, Yang L, Hou B, Zhang M, wu M, Dong J and Ma X 2025 Recent advances in AlN-based acoustic wave resonators *Micromachines* **16** 205
Ma T, Wang J, Du J and Yang J 2015 Resonances and energy trapping in AT-cut quartz resonators operating with fast shear modes driven by lateral electric fields produced by surface electrodes *Ultrasonics* **59** 14–20
Mashimo T and Oba Y 2022 Performance improvement of micro-ultrasonic motors using the thickness shear mode piezoelectric elements *Sens. Actuators A* **335** 113347
Muramatsu H, Tamiya E and Karube I 1988 Computation of equivalent circuit parameters of quartz crystals in contact with liquids and study of liquid properties *Anal. Chem.* **60** 2142–6
Oliveira Fernandes Moreira P 2015 Timing signals and radio frequency distribution using Ethernet networks for high-energy physics applications *PhD thesis* University College London
Pao S Y, Meng B, Wang J, Lin Z D and Peng T H 2024 The optimization of inverted-mesa type quartz crystal resonators with the consideration of effects of structural parameters *IEEE Ultrasonics, Ferroelectrics, and Frequency Control Joint Symp.* pp 1–4
Pogrebnyak A P and Abdrafikov S N 1992 The development and production of high-quality quartz material for precision crystals *IEEE Frequency Control Symp.* pp 679–82
Ramon C 2014 *Understanding Quartz Crystals and Oscillators* (Artech House)
Saigusa Y 2010 5-quartz-based piezoelectric materials *Advanced Piezoelectric Materials* K Uchino ed (Woodhead Publishing) pp 197–233
Salzenstein P 2016 Recent progress in the performances of ultrastable quartz resonators and oscillators *Int. J. Simul. Multidiscip. Des. Optim* **7** A8
Satani H, Yasuda K, Sohgawa M and Abe T 2022 Temperature characteristics of a thickness shear mode quartz crystal resonator bonded to a support substrate *Appl. Phys. Lett.* **121** 25
Sekimoto H, Watanabe Y, Taniguchi T and Nakazawa M 1991 Analysis of spurious characteristics of rectangular AT-cut quartz resonators using plate equations and a one-dimensional finite element method *IEEE Trans. Electron. Inf. Syst.* **111** 372–7
Sfregola F A, Volpe A, Zifarelli A, Benetti M, Cannatà D, Spagnolo V and Patimisco P 2025 Full-domain 3D digital twin for comprehensive analysis and validation of standing surface acoustic wave generation on $LiNbO_3$ substrate *Adv Mater. Technol.* **11** e01275
Sun H-T, Faccio M, Cantalini C and Pelino M 1996 Impedance analysis and circuit simulation of quartz resonator in water at different temperatures *Sens. Actuators. B: Chem.* **32** 169–73
Wei Z, Hu J, Li Y and Chen J 2022 Effect of electrode thickness on quality factor of ring electrode QCM sensor *Sensors* **22** 5159
Wingqvist G 2010 AlN-based sputter-deposited shear mode thin film bulk acoustic resonator (FBAR) for biosensor applications—a review *Surf. Coat. Technol.* **205** 1279–86
Zhang W, Xu Y, Zhang Z, Jing J, Yao B, Gao L, Xue C and Tian Z 2025 Dual-mode AT-cut quartz resonant pressure sensor for wide pressure and temperature measurement ranges *Sens. Actuators A* **382** 116103
Zhu F, Li P, Dai X, Qian Z, Kuznetsova I E, Kolesov V and Ma T 2021 A theoretical model for analyzing the thickness-shear vibration of a circular quartz crystal plate with multiple concentric ring electrodes *IEEE Trans. Ultrason. Ferroelectr. Freq. Control* **68** 1808–18
Zhu F, Wang B, Dai X-Y, Qian Z-H, Kuznetsova I, Kolesov V and Huang B 2019 Vibration optimization of an infinite circular AT-cut quartz resonator with ring electrodes *Appl. Math. Modell.* **72** 217–29
Zimmermann B, Lucklum R, Hauptmann P, Rabe J and Büttgenbach S 2001 Electrical characterisation of high-frequency thickness-shear-mode resonators by impedance analysis *Sens. Actuators B* **76** 47–57